A 2 ½-D finite element method to model borehole effects on density log

Jadir da Conceição da Silva*, UFRJ – Departamento. de Geologia/IGEO/CCMN

Abstract

Measurement of formation densities is well established by logs, but a difficulty remains for computation of environmental effects that seriously affect log interpretations. In this paper, I develop a theoretical model based on the finite element method (FEM) to simulate the gamma - gamma spectral density log for radially symmetric media. My approach is based on the known Galerkin technique. The computed parameter is the scalar flux from the multigroup diffusion approximation of Boltzmann transport equation (BTE). The method is used to theoretically determine densities of complex lithological sequences. Examples of synthetic logs show the usefulness of this kind of numerical modeling for studying important effects in the density logs such as borehole size, mud weight and invasion. Results indicate FEM as an accurate and computationally efficient method to predict all these significant environmental effects affecting the density tool responses.

Intrduction

Subsurface density formation is one important petrophysical parameter for up-to-date interpretation of geophysical data and formation evaluation. In surface seismic prospecting, density is a basic parameter to compute layer's acoustic impedance. The spectral borehole gamma - gamma density tool may be used for density evaluation. It is constituted by a collimated gamma ray source (usually Cs^{137}) that impinges radiation in borehole-surrounded formation and detects radiation scattered back into two detectors in the tool itself, located at 15 and 32 cm from the point source. At sufficiently high energies (150 to 500 keV) Compton scattering predominates (Bertozzi et al., 1981). The average electron density in a small volume of rock controls the counting rate of the scattered radiation. This average electron density strongly correlates with formation bulk density (Meyers, 1992).

The goal of this paper is to simulate, by the finite-element method (FEM), the transport of gamma radiation emitted by the Cs^{137} point source and its interaction with formation material. The accuracy of the FEM is tested comparing its results with the analytical solution obtained from a simple model (Tittle e Allen, 1966). An additional test is performed to achieve the best convergent result concerning the ideal number of energy groups. To accurately apply these ideas, requires the use of proper geological and mathematical models of the system under study. The mathematical model is that suggested by the Boltzmann transport equation, which, in a cylindrical coordinate system for a radially symmetric media, assumes the following form

$$-\frac{1}{\rho}\frac{\partial}{\partial\rho}\left(\rho D_g\frac{\partial\Phi_g}{\partial\rho}\right)-\frac{\partial}{\partial z}\left(D_g\frac{\partial\Phi_g}{\partial z}\right)+\Sigma_{T,g}\Phi_g = \sum_{g'=1}^{g-1}b_{gg'}\Phi_{g'}+\frac{S_g\delta(\rho)\delta(z-z_0)}{2\pi\rho}, \quad (1)$$

with known boundary conditions. The index g denotes the group and diffusion coefficient, D_g, total reaction cross-section, Σ_T, and transition matrix elements, $b_{gg'}$, are functions only of the spatial coordinates.

Mathematical aspects of the FEM algorithm

General considerations of the finite element solution of the system of equations (1) consist basically in subdividing the region surrounding the well in a set of triangular elements which constitute the FEM mesh (Davies, 1980) Next, the required scalar gamma ray flux is approximated within each of these elements by a linear interpolation function

$$\widetilde{\Phi}^{(e)} = \Phi_1 L_1^{(e)} + \Phi_2 L_2^{(e)} + \Phi_3 L_3^{(e)} + \cdots, \quad (2)$$

where $L_j^{(e)}$ is a base function defined by

$$L_j^{(e)} = a_j + b_j\rho + c_j z. \quad (3)$$

As expansion defined by equation (2) must be finite, an approximation error ε results, given by

$$\varepsilon = \mathbf{K}^{(e)}\widetilde{\Phi}^{(e)} - \mathbf{f}^{(e)}, \quad (4)$$

where $\mathbf{K}^{(e)}$ is the local stiffness matrix associated with element (e) of the FEM mesh and $\mathbf{f}^{(e)}$ is the source vector quantity. The goal of the FEM is to minimize this error. To perform this task it is necessary to take the inner product of the error and a test function $\mathbf{N}_n^{(e)}$ be zero over the region where the local base function is defined,

General considerations of the finite element solution of

$$\left\langle \mathbf{N}_n^{(e)}, \varepsilon \right\rangle = \iint_{(e)} \mathbf{N}_n^{(e)}\varepsilon d\rho dz = 0 \text{ for } n = 1,2,3. \quad (5)$$

Mathematically, this means that the error is orthogonal to the test function into the sub domain (e). Amongst several strategies to built approximated solutions of the boundary values problems I have chosen the *Galerkin* method

where the base and test functions are equal, $N_n^{(e)} = L_n^{(e)}$. So, the norm ||ε|| is minimized by this method.

The stiffness matrix

By applying the Galerkin method on the first and second terms of the left-hand side of equation (1) one has defined the first term of the stiffness matrix

$$K_{ij,(1)}^{(e)} = \iint_{A_e} D_g(\rho,z)\frac{\left(b_i b_j + c_i c_j\right)}{4A_e^2} 2\pi\rho d\rho dz \text{ for} i,j = 1,2,3, \qquad (6)$$

where A_e is the area of the element (e). If the parameter $D_g^{(e)}$ (ρ, z) is the diffusion coefficient for element (e), equation (6) results in

$$K_{ij,(1)}^{(e)} = \frac{\pi\bar{\rho}D_g^{(e)}}{2A_e}\begin{bmatrix} b_1^2+c_1^2 & b_1b_2+c_1c_2 & b_1b_3+c_1c_3 \\ b_2b_1+c_2c_1 & b_2^2+c_2^2 & b_2b_3+c_2c_3 \\ b_3b_1+c_3c_1 & b_3b_2+c_3c_2 & b_3^2+c_3^2 \end{bmatrix} \qquad (7)$$

where the medium radius is $\bar{\rho}$ = (ρ1 + ρ2 + ρ3)/3. The third term on the left-hand side of equation (1) define the second term of the local stiffness matrix

$$K_{ij,(2)}^{(e)} = 2\pi\Sigma_{T,g}^{(e)} \iint_{A_e} \rho L_i^{(e)} L_j^{(e)} d\rho dz. \qquad (8)$$

By also expanding the radius ρ in the base functions $L_i^{(e)}$ and defining

$$\iint_{A_e} L_i^m L_j^n L_k^l dA = \frac{m!n!l!}{(m+n+l+2)!} 2A_e \qquad (9)$$

and

$$\Delta = \frac{\pi\Sigma_{T,g}^{(e)} A_e}{5}, \qquad (10)$$

one finds all elements of equation (8):

$$K_{11,(2)}^{(e)} = \Delta\left(\bar{\rho} + 2\frac{\rho_1}{3}\right),$$

$$K_{12,(2)}^{(e)} = \Delta\left(\bar{\rho} - \frac{\rho_3}{6}\right) = K_{21,(2)}^{(e)},$$

$$K_{13,(2)}^{(e)} = \Delta\left(\bar{\rho} - \frac{\rho_2}{6}\right) = K_{31,(2)}^{(e)},$$

$$K_{22,(2)}^{(e)} = \Delta\left(\bar{\rho} + 2\frac{\rho_2}{3}\right), \qquad (11)$$

$$K_{23,(2)}^{(e)} = \Delta\left(\bar{\rho} + \frac{\rho_1}{6}\right) = K_{32,(2)}^{(e)}$$

and

$$K_{33,(2)}^{(e)} = \Delta\left(\bar{\rho} + 2\frac{\rho_3}{3}\right).$$

So, the stiffness matrix of the FEM local system has been determined as

$$\mathbf{K}^{(e)} = \mathbf{K}_{(1)}^{(e)} + \mathbf{K}_{(2)}^{(e)}. \qquad (12)$$

The source vector

Identical to the stiffness matrix, the source vector is also constituted by two terms. The first one is provided by all photons coming from the higher energy groups g' that have acquired energy sufficient to be included in the group g, i.e.,

$$F^{(e)}(\rho,z) = \sum_{g'=1}^{g} b_{gg'}(\rho,z)\Phi_{g'}^{(e)}(\rho,z), \qquad (13)$$

and so

$$f_{i,(1)}^{(e)} = \iint_{A_e} F^{(e)}(\rho,z) L_i^{(e)} 2\pi\rho d\rho dz \text{ for } i = 1,2,3. \qquad (14)$$

Expanding both transition source $F^{(e)}$(ρ, z) and ρ in base function $L_i^{(e)}$, the first source term is given by

$$f_{i,(1)}^{(e)} = 2\pi\iint_{A_e}\begin{bmatrix} L_1^{(e)} & L_2^{(e)} & L_3^{(e)} \end{bmatrix}\begin{bmatrix} F^{(e)}(\rho_1,z_1) \\ F^{(e)}(\rho_2,z_2) \\ F^{(e)}(\rho_3,z_3) \end{bmatrix}\begin{bmatrix} \rho_1 & \rho_2 & \rho_3 \end{bmatrix}\begin{bmatrix} L_1^{(e)} \\ L_2^{(e)} \\ L_3^{(e)} \end{bmatrix} L_i^{(e)} d\rho dz \qquad (15)$$

By solving equation (15), one has

$$f_{1,(1)}^{(e)} = \frac{1}{30}[6\alpha + \eta + 2(\beta+\gamma+\chi+\lambda)],$$

$$f_{2,(1)}^{(e)} = \frac{1}{30}[6\beta + \lambda + 2(\alpha+\gamma+\chi+\eta)], \qquad (16)$$

and

$$f_{3,(1)}^{(e)} = \frac{1}{30}[6\gamma + \chi + 2(\alpha+\beta+\lambda+\eta)],$$

where $\alpha=\pi\rho_1 S_1 A_e$, $\beta=\pi\rho_2 S_2 A_e$, $\gamma=\pi\rho_3 S_3 A_e$, $\chi=\pi(\rho_1 S_2 + \rho_2 S_1)A_e$, $\lambda=\pi(\rho_1 S_3 + \rho_3 S_1)A_e$ and $\eta=\pi(\rho_2 S_3 + \rho_3 S_2)A_e$. The second term of the source vector refers to the Cs^{137} point source. When the *Galerkin* technique is applied to it, one obtains the following expression

$$f_{i,(1)}^{(e)} = \iint_{A} \frac{S_g \delta(\rho)\delta(z-z_0)}{2\pi\rho} L_i 2\pi\rho d\rho dz. \qquad (17)$$

Based on the properties of the Delta Dirac function, only that node in the global source vector contains the point source S (ρ=0, z=z_0), i.e.,

$$\mathbf{f}_{(2)} = \begin{bmatrix} \vdots \\ S \\ \vdots \end{bmatrix}. \qquad (18)$$

Last, the local stiffness matrix and source vector quantities are assembled into their global configuration,

$$\mathbf{K} = \sum_{e} \mathbf{K}^{(e)} \tag{19}$$

and

$$\mathbf{f} = (\sum_{e} \mathbf{f}_{(1)}^{(e)}) + \mathbf{f}_{(2)} \tag{20}$$

which results in the following global system of the finite element method

$$\mathbf{K\Phi} = \mathbf{f}. \tag{21}$$

Any class of efficient numerical algorithm, accounting for the relevant sparseness and bandwidth structure of the matrix **K**, can now be used to solve equation (21) for scalar flux.

Analysis of convergence

The results obtained by the FEM have been checked quite extensively against analytical solution for the scalar flux in limiting cases (Tittle e Allen, 1966). I have suggested a new approach to get a convergent solution for gamma radiation, which consists in increasing the number of terms of the series solution until one has obtained the required convergent solution. The summation starts with 11 points. Figures 1(A) and 1(B) indicate that number is insufficient to establish the required convergence for both vertical and radial axis.

However, the problem was solved by increasing step by step the number of series terms, namely 101, 201 and 301. Solutions for terms between 201 and 301 have suggested this last as a rather ideal number of terms to check our FEM solution, as verified by Figures 1(C) and 1(D). To additionally verify the convergence of the numerical solution, when the number of energy groups in the multigroup diffusion approximation is increased, a specified limit of energies groups, say 100, is given. This number was considered sufficient to get a convergent solution. I have found that for z = 15cm and 32cm, which correspond to the near and far detector locations, it is necessary at least 50 energy groups to reach convergence.

Mud weight effects

Figure 2(A) shows the FEM synthetic log from a horizontally geological layered model constituted by five planar layers with thicknesses of 40cm each. The layers L1, L3 and L5 correspond to a 40% porosity sandstone with 60% of quartz and 40% water-saturated. Layers L2 and L4 have 10% porosity, and are a mixture of evaporite and carbonate. Volumetric mineral fractions are 20% of calcite, 20% of dolomite, 50% of anhydrite and a 10% water saturated porosity. Two kinds of borehole fluids are simulated, fresh water and a mixture of 10% of barite and 90% of water. For water-based mud one observes that all layer interfaces are accurately recognized. The values of simulated and true densities show excellent agreement and have demonstrated the attainable accuracy and precision of the FEM modeling. The agreement occurs mainly because this model has the same mud and well bore composition as that of the hypothetical calibration model used to compute the constants. On the other hand the log simulated with barite-based mud shows higher density values, reflecting the higher barite density. In such case, one can not identify with sufficient accuracy most of the layers´ interfaces. The density values on the center of layers L2 and L4 are about 18.7% higher than the true densities. For L1, L3 and L5 these values are only 6.22% higher. So, I have concluded that mud density strongly influence the interface locations with gamma-gamma density logs.

Thin layers response

In order to simulate thin layers effects on the density tool response I have employed again a geological horizontally layered model composed by twelve planar layers. Figure 2(B) illustrates the synthetic log concerning such model. Layer L1 is an evaporite with thickness of 40cm and constituted by 90% of anhydrite and 10% water-saturated porosity. Layer L2 is a mixture of evaporites and carbonate with 20% of calcite, 20% of dolomite, 50% of anhydrite and 10 % water-saturated porosity. At depths ranging from 70cm to 190 cm occurs a sequence of eight thin layers labeled L3 to L10 each of which are 15cm thick. Layers L3, L5, L7 and L11 are sandstones with volumetric mineral fraction given by 60% of quartz and 40% of water porosity. Layers L4, L6, L8, L10 and L12 are a 40% porosity mixture of evaporite and carbonate. The log in this region exhibits an oscillatory pattern characteristic of a cyclical material deposition in a low-energy environment. Due to the low density contrast between L1 and L2, associated with a high contrast between L2 and L3, the layer L2 is not distinguishable on the log. This observation suggests the existence of a unique thicker layer extending from the top of the model until a depth of 70cm.

Invasion effects

To model the influence of invasion effects on density logs a geological horizontally layered model was used, composed by three planar layers with thickness of 50cm. The layers L1 and L3 are a 35% porous formation with 10% of quartz, 20% of calcite, 20% of dolomite, 15% of feldspar and 35% of oil-saturated porosity. The central layer L2 is a 20% porosity sandstone with 80% of quartz and 20% of water-saturated porosity. This layer is supposed permeable enough to allow an invasion radius up to 10cm. The resulting synthetic logs are illustrated in Figure 2(C). Invasion effects at the mid-point of this layer result in a density 1.8 % lower than its correspondent water log. This unusual exchange in density values occurs because the lithology does not correspond to that of the calibration model. Additionally I have imposed a displacement of oil by the water mud in the invasion zone which means an increasing in density near the borehole wall. It was also verified a surprising better fitting for no invasion log. Finally, I have observed that the invasion effects do not influence the interfaces´ position determination.

Washout effects

To illustrate the washout effects on density logs I have proposed a geological model constituted by three horizontal layers with thickness of 100cm (Figure 2(D)).

The layers L1 and L3 are a sandstone composed by 60% of quartz and 40% of water-saturated porosity. The central layer L2 is shale with 10% of quartz, 20% of illite, 20% of montmorillonite and 20% of water-saturated porosity. Also, in the central layer were imposed three wall overbreaks ranging from depths of 120-135cm, 150-165cm and 180 - 200cm. Each of them results in a well diameter enlargement of 20%. The normal synthetic log shown in Figure 2(D) is quite accurate provided its similarity with the calibration model. The washout log exhibits similar aspects in the curves acquired from a sequence of thin bed showing significant density contrast. At depth of 200cm there is evidence of a displacement of the original interface location due to a drift in the log caused by a 20cm thick overbreak that falls exactly on this interface.

Conclusions

The finite-element method (FEM) was applied to simulate the gamma-gamma spectral density log in geological horizontally layered models. I have shown that FEM is accurate and computationally efficient in predicting density tool responses. The washout effect is the main cause of oscillations in the gamma-gamma density log within a homogeneous layer. Most of thin layers sequence results in a pattern often recognized in cyclic sedimentation processes. I have observed that different mud densities affect the interface locations while invasion effects have only scant influences in these locations. Borehole overbreak may cause drift in interface positions, what can make some of them indistinct in the density logs.

Acknowledgement

The computational facilities that helped the preparation of this manuscript were provided by the PRH-18 / ANP-UFRJ and Fundação de Amparo à Pesquisa do Estado do Rio de Janeiro (FAPERJ) through Research Project E-26/171.521/98.

References

Bertozzi, W., Ellis, V., Wahl, J. S., The physical foundation of formation lithology logging with gamma rays, *Geophysics*, V.46, p.1439 – 1455, 1981.

Davies, A. L., The finite element method: a first approach, Claredon Press, 1980.

Meyers, G. D., A review of nuclear logging, *The Log Analyst*, V.34, p.228-238, 1992.

Tittle, C. W., Allen, L. S., Theory of neutron logging II, Geophysics, V.31, p.214-224, 1996.

Tittman, J., Whal, J. S., The physical foundation of formation density logging (gamma-gamma), *Geophysics*, V.30, p.284-294, 1965.

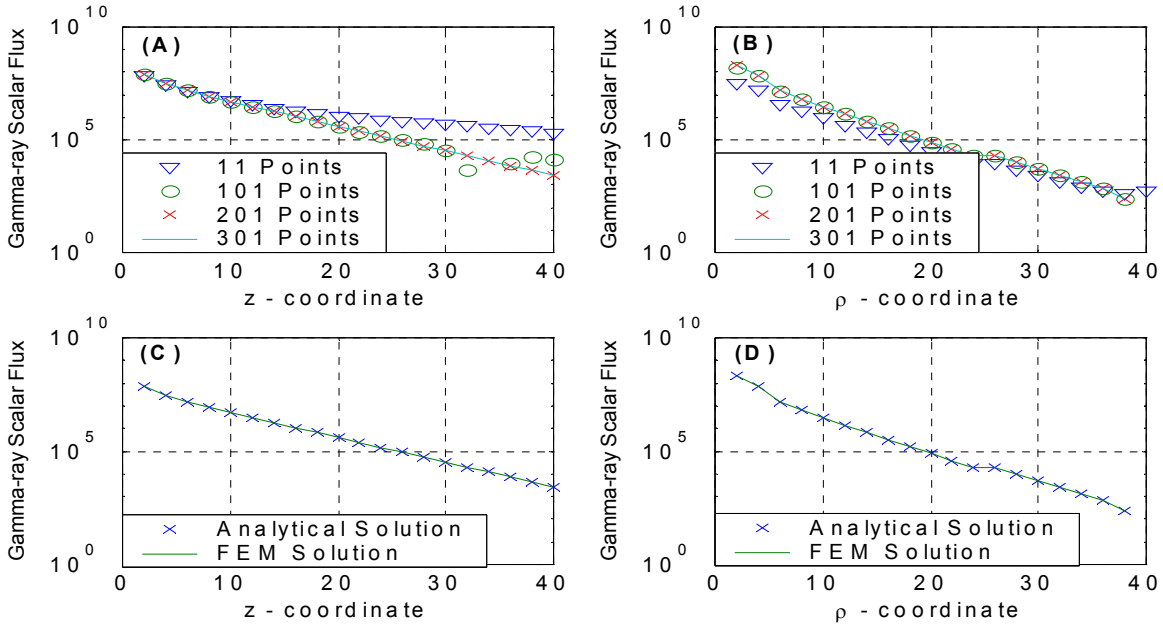

Figure 1: **(A)** Analysis of Convergence in the z-coordinate; **(B)** Analysis of Convergence in the ρ-coordinate; **(C)** Results by comparing analytical and numerical solutions in the z-coordinate and **(D)** Results by comparing analytical and numerical solutions in the ρ-coordinate.

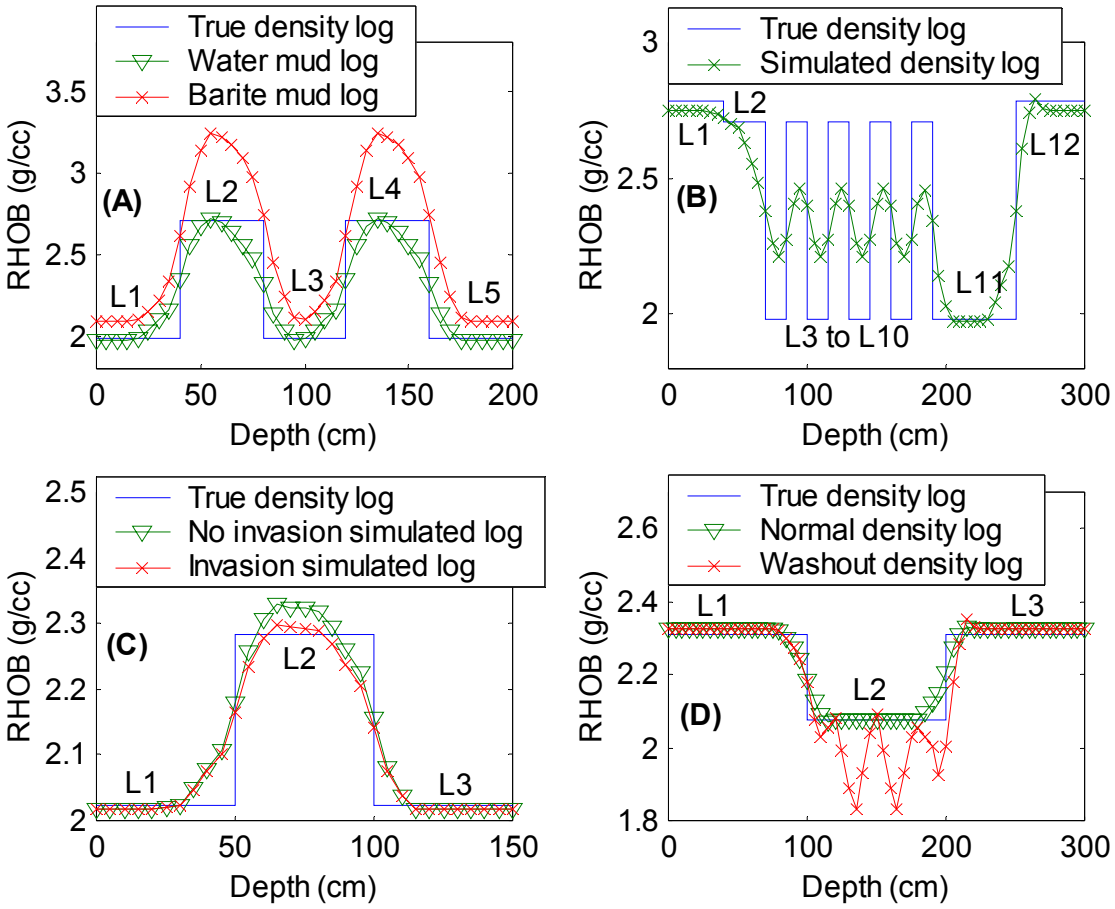

Figure 2: **(A)** Example of mud weight effects on density log; **(B)** Example of thin layers response on density log; **(C)** Example of invasion effects on density log and **(D)** Example of washout effects on density log.